



1 Ammonia emission estimates using CrIS satellite observations over
2 Europe

3 Jieying Ding^{1*}, Ronald van der A¹, Henk Eskes¹, Enrico Damers², Mark Shephard³, Roy
4 Wichink Kruit⁴, Marc Guevara⁵, Leonor Tarrason⁶

5 1. Royal Netherlands Meteorological Institute (KNMI), De Bilt, The Netherlands

6 2. Netherlands Organisation for Applied Scientific Research (TNO), Utrecht, The Netherlands

7 3. Environment and Climate Change Canada (ECCC), Toronto, Ontario, Canada

8 4. National Institute for Public Health and the Environment, Bilthoven, The Netherlands

9 5. Barcelona Supercomputing Center, Barcelona, Spain

10 6. NILU – Norwegian Institute for Air Research, Kjeller, Norway

11

12 *Corresponding authors: Jieying Ding (jieying.ding@knmi.nl)

13

14

15 Abstract

16

17 Over the past century ammonia (NH₃) emissions have increased with the growth of livestock and
18 fertilizer usage. The abundant NH₃ emissions lead to secondary fine particulate matter (PM_{2.5})
19 pollution, climate change, reduction in biodiversity and affects human health. Up-to-date and spatially
20 and temporally resolved information of NH₃ emissions is essential to better quantify its impact. In this
21 study we applied the existing DECSO (Daily Emissions Constrained by Satellite Observations)
22 algorithm to NH₃ observations from the Cross-track Infrared Sounder (CrIS) to estimate NH₃ emissions.
23 Because NH₃ in the atmosphere is influenced by Nitrogen Oxides (NO_x), we implemented DECSO to
24 estimate NO_x and NH₃ emissions simultaneously. The emissions are derived over Europe for 2020 on a
25 spatial resolution of 0.2° × 0.2° using daily observations from both CrIS and TROPOMI (on the Sentinel
26 5p satellite). Due to the sparseness of daily satellite observations of NH₃, monthly emissions of NH₃ are
27 reported. The total NH₃ emissions derived from observations are about 8 Tg/year with a precision of
28 about 0.2 % over the European domain. The comparison of the satellite-derived NH₃ emissions from
29 DECSO with independent bottom-up inventories and in-situ observations indicates a consistency in



30 terms of magnitude on the country totals, the results also being comparable regarding the temporal and
31 spatial distributions.

32

33

34 1 Introduction

35

36 Ammonia (NH₃) is the most abundant alkaline gas and one of the main reactive nitrogen species in the
37 atmosphere. NH₃ is a precursor for the formation of atmospheric aerosols, which play an important role
38 in climate change. In Europe, about 50% (Wyer et al., 2022) of atmospheric NH₃ is transformed into
39 fine particulate matter (PM_{2.5}) composed of ammonium through chemical reactions with sulfuric and
40 nitric acids from nitrogen oxides (NO_x) and sulphur dioxides (SO₂) in the atmosphere (Renard et al.,
41 2004; Schaap et al., 2004). According to the European Environment Agency (EEA), the dominant
42 source of NH₃ in Europe is agriculture, which was responsible for more than 90% of the European
43 emissions. The other source sectors include industry, transport, energy, waste treatment and biomass
44 burning (Behera et al., 2013; Backes et al., 2016a; Van Damme et al., 2018; Adams et al., 2019).
45 Excessive NH₃ emissions have adverse impact on biodiversity, human health, and climate change
46 (Galloway et al., 2008). Over the past century, NH₃ emissions increased strongly with the growing
47 human population, cattle farming and fertilizer usage (Crippa et al., 2023; Erisman et al., 2008; Van
48 Damme et al., 2021), leading to high nitrogen deposition loads to water and soil (Erisman et al., 2013)
49 with the associated eutrophication, acidification and biodiversity loss problems (Behera et al., 2013).
50 Since 2019, the Dutch policy makers paid a lot of attention to NH₃ emissions due to the nitrogen (N)
51 crisis after the national programmatic approach to nitrogen was rejected by the supreme court, because
52 it was inadequate for the protection of vulnerable nature areas (Natura2000). The Dutch government is
53 obliged by EU laws to protect the natural environment and prevent damage caused by too high
54 emissions of reactive nitrogen. Studies shows that abatement of NH₃ emissions is very cost-effective to
55 improve air quality and have high social benefits (Backes et al., 2016b; Zhang et al., 2020; Gu et al.,
56 2021). Detailed spatially and temporally resolved information of NH₃ emissions is crucial for both
57 scientific communities and policy makers to study and predict pollutant concentrations and deposition
58 with their impact on the environment and to motivate environmental control strategies.

59 The empirical method to estimate NH₃ emissions is the so-called bottom-up approach, which combines
60 available official reported activity data incorporating a full differentiation of emission activities with
61 emission factors, and technology and abatement measures from individual countries for each source
62 category (Crippa et al., 2018; Crippa et al., 2023; Janssens-Maenhout et al., 2019). The annual emissions
63 are then distributed in time and space based on proxy data such as land use data, and meteorological



64 parameters (Backes et al., 2016a). Ge et al. (2020) summarized the key factors of agricultural NH₃
65 emissions: local agricultural practices, method of manure and fertilizer application including type,
66 amount and method, animal type, housing type, manure storage type, meteorological conditions, soil
67 conditions, and regulation of agricultural practice. The uncertainties of NH₃ emissions calculated by the
68 bottom-up approach are very large due to insufficient data on agricultural activities (Behera et al., 2013;
69 Beusen et al., 2008). Crippa et al. (2018) pointed out that the uncertainty of NH₃ (between 186 % and
70 294.4 %) in the EDGAR (The Emissions Database for Global Atmospheric Research) inventory is the
71 largest among all pollutants because of the high uncertainty of both agricultural statistics and emission
72 factors.

73 The validation of NH₃ emission inventories using ground-based observations is very challenging due
74 to the sparsely distributed in-site measurement network. NH₃ concentrations have large temporal and
75 spatial variability due to its short lifetime, which ranges from about a few hours to two days (Dammers
76 et al., 2019; Luo et al., 2022). Densely distributed hourly or daily ground measurements are impractical
77 for large areas due to high costs and specific operational requirements (Noordijk et al., 2020). In the
78 last decade, a wide spatial and temporal coverage of satellite observations of NH₃ in lower troposphere
79 was established due to the development of infrared nadir viewing satellite instruments, such as the
80 Tropospheric Emission Spectrometer (TES) (Beer et al., 2008) on the NASA Aura satellite. The
81 operational Cross-track Infrared Sounder (CrIS) (Shephard and Cady-Pereira, 2015) on the Suomi
82 National Polar-orbiting Partnership (S-NPP) and on the Joint Polar Satellite System-1 and System-2
83 (JPSS-1 and JPSS-2) satellites of NASA/NOAA, and the Infrared Atmospheric Sounder Interferometer
84 (IASI) (Clarisse et al., 2009) on the MetOp satellites from the European Space Agency (ESA), with
85 their large swaths, provide daily global coverage of NH₃ observations and improve our understanding
86 of NH₃ global distribution and temporal variability.

87 NH₃ emissions can be obtained by applying an inversion algorithm to satellite observations. Such
88 estimates provide useful information which is independent from bottom-up inventories. By using IASI
89 NH₃ observations, Van Damme et al. (2018) identified NH₃ emission hotspots and calculated emissions
90 based on a mass balance approach. They found that NH₃ emissions of most hotspots, especially
91 industrial emitters, were largely underestimated compared to EDGAR. Dammers et al. (2019) used both
92 IASI and CrIS observations to derive emissions, lifetimes and plume widths of NH₃ from large
93 agricultural and industrial point sources and concluded that 55 locations were missing in the
94 Hemispheric Transport Atmospheric Pollution version 2 (HTAPv2) emission inventory. Besides the
95 studies on point sources, data assimilation techniques combining a chemical transport model (CTM)
96 with satellite observations are also widely used to derive NH₃ surface emissions. van der Graaf et al.
97 (2022) adjusted the NH₃ emissions over Europe using a local ensemble transport Kalman filter (LETKF)
98 applied to CrIS NH₃ profiles. Sitwell et al. (2022) developed an ensemble-variational inversion system
99 to estimate NH₃ emissions from CrIS over North America. Another widely used method is 4D-Var



100 using the GEOS-Chem global chemistry transport model, which has been applied to America, China
101 and Europe using NH₃ observation from different instruments (Zhu et al., 2013; Zhang et al., 2018; Li
102 et al., 2019; Cao et al., 2020; Chen et al., 2021; Cao et al., 2022). The main advantage of CrIS is the
103 combination of global coverage and the improved sensitivity in the boundary layer attributed to the low
104 spectral noise of about 0.04 K at 280 K in the NH₃ spectral band (Zavalyov et al., 2013). The infrared
105 instrument is also more sensitive at the overpass time in the early afternoon with high thermal contrast
106 between air and surface.

107 The Daily Emissions Constrained by Satellite Observations (DECSO) inversion algorithm uses satellite
108 column observations to derive emissions for short-lived gases based on an extended Kalman Filter
109 (Mijling and van der A, 2012). The concentrations of the species are calculated from the emissions by
110 a CTM and compared to satellite observations. One of the main advantages to use DECSO is the fast
111 calculation speed compared to other data assimilation methods. Furthermore, the derived emissions are
112 updated by addition, not by scaling the existing emissions. This enables the fast detection of new sources
113 and changed emissions. In previous studies, DECSO has been applied to nitrogen dioxide (NO₂)
114 observations from different satellites and uses the Eulerian regional off-line CTM CHIMERE (Menut
115 et al., 2021; Menut et al., 2013) to estimate regional NO_x (NO₂+NO) emissions and it revealed that the
116 temporal and spatial variability of total surface NO_x emissions are well captured by DECSO compared
117 to bottom-up inventories or in-situ observations (Ding et al., 2015; Ding et al., 2017b; Ding et al., 2020;
118 van der A et al., 2020; Ding et al., 2022; Liu et al., 2018; van der A et al., 2024).

119 Direct validation of emission inventories, regardless of bottom-up or satellite-derived approaches,
120 presents the same challenge due to the inherent difficulty of directly measuring large-scale emissions
121 on the ground. The intercomparison of emissions using independent data and different approaches are
122 usually performed to assess the emission data. Another common way to validation emissions can be
123 achieved by using them as input data in a chemical transport model. The model simulated concentrations
124 are compared to in-situ observations.

125 In this study we extend the DECSO-NO_x system to NH₃ in order to derive both NO_x and NH₃ emissions
126 simultaneously, using CrIS NH₃ observations and NO₂ observations from the TROPospheric
127 Monitoring Instrument (TROPOMI) (Veefkind et al., 2012). Using the multi-species DECSO version,
128 we update NO_x and NH₃ emissions simultaneously to reduce the impact of the temporal change (e.g.
129 trend) of NO_x when deriving NH₃ emissions. After the description of the DECSO algorithm applied to
130 NH₃, the results of NH₃ emissions over Europe are presented at a spatial resolution of 0.2° × 0.2°. To
131 evaluate the derived NH₃ emissions, we will compare the country totals and the monthly variability
132 with bottom-up inventories with a focus on NH₃ emissions in the Netherlands. In addition, we compare
133 the NH₃ concentration simulations of CHIMERE using different emission inventories with in-situ
134 observations.



135

136 2 Data and Method

137 2.1 Satellite observations

138 2.1.1 CrIS observations of NH₃

139 The CrIS instrument is a Fourier transform spectrometer (FTS) launched on the Suomi National Polar-
140 orbiting Partnership (SNPP) satellite in 2011 and on the NOAA-20 satellite in 2017. The overpass time
141 of SNPP at the equator is about 01:30 and 13:30 local time. NOAA-20 circles the earth in the same orbit
142 as SNPP, but it is separated in time and space by 50 minutes and crosses the equator at about 02:20 and
143 14:20 local time. The instrument has a wide swath of up to 2200 km providing twice daily global
144 coverage. The total angular field-of-view consists of a 3×3 array of circular pixels of 14 km diameter
145 each at nadir (Han et al., 2013). CrIS measures the infrared spectrum including the main NH₃ spectral
146 signatures located in the longwave window region between 900 and 1000 cm⁻¹. The spectral resolution
147 of the radiance data is 0.625 cm⁻¹. NH₃ observations are retrieved with the CrIS Fast Physical Retrieval
148 (CFPR) algorithm based on an optimal estimate method minimizing the difference between measured
149 spectral radiances and those simulated by a radiative transfer model (Shephard and Cady-Pereira, 2015).
150 Three typical a priori profiles of NH₃ representing high-source, moderate-source and background source
151 are used in the retrieval algorithm. The NH₃ profile are retrieved on 14 pressure levels with the peak
152 sensitivity of CrIS between 900 and 700 hPa (Shephard et al., 2020). We use the version 1.6.4 retrieval
153 products of CrIS on both SNPP and NOAA-20 from September 2019 to December 2020, which also
154 accounts for non-detects in the observations and retrievals through optically thin clouds (White et al.,
155 2023). We use the daytime observations with the quality flag larger than 3 over our study domain of
156 Europe [-10° ~30° E, 35° ~ 55° N] (Shephard et al., 2020). Since there are almost no emissions over
157 ocean, we only use the observations over land. To reduce extreme emission updates in one day we filter
158 the NH₃ data larger than the value at 99th percentile of all observations for the selected period over the
159 study domain. This has also been applied by van der Graaf et al. (2022). To make a fair comparison
160 between NH₃ observations of CrIS and model simulations of CHIMERE, we interpolate modelled
161 concentrations from the model grid cell over the satellite footprints and apply the averaging kernel to
162 the modelled profile. Although the NH₃ observations from CrIS are in circular pixels, we still assume
163 the pixel to be rectangular and calculate the pixel corner coordinates based on the satellite height,
164 satellite zenith angle and viewing angle assuming the width of the pixel to be equal to the diameter of
165 the circular pixel. To simplify the calculation of applying the original logarithmic averaging kernels,
166 we converted them to linearized average kernels based on the method of Cao et al. (2022).

167



168 *2.1.2 TROPOMI observations of NO₂*

169 TROPOMI is onboard the Sentinel-5 Precursor (S5P) satellite launched on 13 October 2017 with the
170 high spatial resolution of $3.5 \times 5.5 \text{ km}^2$ at nadir for the NO₂ observations. The overpass time is about
171 13:30 local time, similar as for CrIS. We use TROPOMI tropospheric NO₂ columns from the version
172 2.4 reprocessed retrieval dataset (van Geffen et al., 2022) and follow the recommendations for using
173 the QA value as detailed in the Product User Manual (Eskes and Eichmann, 2022). NO₂ columns are
174 converted into ‘superobservations’ representing the integrated average (Boersma et al., 2016; Rijdsdijk
175 et al., 2024) over the $0.2^\circ \times 0.2^\circ$ grid cells. In this paper, the superobservations are calculated for the
176 NO₂ columns from surface till about 700hPa where the NO₂ concentrations are most related to surface
177 emissions. The details of TROPOMI NO₂ data used by DECSO are described in Ding et al. (2020) and
178 van der A et al. (2024).

179

180 *2.2 Ground-based observations.*

181 To evaluate the NH₃ emissions derived by DECSO, we use independent ground-based observations in
182 2020 to compare with model simulated NH₃ concentrations of CHIMERE using different inventories.
183 Compared to other countries, Netherlands has the densest network for monitoring surface NH₃
184 concentrations. We use hourly NH₃ concentrations measured by mini-DOAS at six locations (Figure S1)
185 from the Dutch Monitoring Air Quality (LML) network (Berkhout et al., 2017) and monthly
186 measurements of NH₃ concentration provided by passive samples at 394 locations (Figure S2) from the
187 Dutch Measuring Ammonia in Nature (MAN) network (Lolkema et al., 2015). The uncertainty in NH₃
188 concentrations measured with individual passive samples is large and the measurements are calibrated
189 monthly against the high-quality measurements from the LML network to enhance the accuracy.

190

191 *2.3 Emission inventories*

192 To verify the satellite-derived emissions of NH₃ in Europe, we compare them to several emission
193 inventories including: the national emissions inventories officially reported under the Convention on
194 Long-range Transboundary Air Pollution (LRTAP) (Pinterits, 2023) of 2020, the emissions reported
195 under the European Pollutant Release and Transfer Register (E-PRTR) (EPTR, 2012) of 2020
196 including releases from industrial facilities and livestock facilities, the global emission inventory
197 Hemispheric Transport of Air Pollution (HTAP) v3 of 2018 (Crippa et al., 2023), the Copernicus
198 Atmosphere Monitoring Service (CAMS) Global anthropogenic emissions (CAMS-GLOB-ANT) v5.3
199 of 2020 (Soulie et al., 2023), the regional European CAMS anthropogenic emission inventory (CAMS-
200 REG-ANT) v5.1 of 2020 (Kuenen et al., 2022) and the Dutch official registered emissions of NH₃ in
201 2020 (<https://data.emissieregistratie.nl/export>) (see Table 1). HTAP v3 has been developed by



202 integrating official inventories over specific areas including CAMS-REG-ANT v5.1 for Europe with
 203 the EDGAR v6.1 inventory for the remaining world regions with the spatial resolution of $0.1^\circ \times 0.1^\circ$.
 204 CAMS-GLOB-ANT combines the EDGAR annual emissions and the Copernicus Atmosphere
 205 Monitoring Service TEMPORal profiles (CAMS-TEMPO) on a global scale (Guevara et al., 2021). The
 206 emissions of the most recent years are calculated based on the trends from the Community Emissions
 207 Data System (CEDS) global inventory (Hoesly et al., 2018). The resolution of CAMS-GLOB-ANT is
 208 $0.1^\circ \times 0.1^\circ$. CAMS-REG-ANT v5.1 provide yearly emissions on the spatial resolution of $0.1^\circ \times 0.05^\circ$.
 209 We have applied the regional European CAMS-TEMPO profiles (Guevara et al., 2021) to CAMS-REG-
 210 ANT v5.1 to get the monthly emissions (hereinafter referred to as CAMS-REG-TEMPO). The Dutch
 211 registered NH_3 emissions are taken from <https://www.emissieregistratie.nl> and provided annually on a
 212 high resolution of $1 \text{ km} \times 1 \text{ km}$. To compare the derived NH_3 emissions of DECSO spatially with
 213 bottom-up inventories, we aggregate emissions from these bottom-up inventories into the $0.2^\circ \times 0.2^\circ$
 214 grid cells of the DECSO working domain.

215

216 *Table 1. Summary of the bottom-up inventories compared to the satellite-derived NH_3 emissions from DECSO.*

Emission inventory	Year	Spatial Resolution	Temporal resolution
LRTAP	2020	Country total	Annual
E-PRTR	2020	Point source	Annual
HTAP v3	2018	$0.1^\circ \times 0.1^\circ$	Monthly
CAMS-GLOB-ANT v5.3	2020	$0.1^\circ \times 0.1^\circ$	Monthly
CAMS-REG-ANT v5.1	2020	$0.1^\circ \times 0.05^\circ$	Annual, monthly (with CAMS-REG-TEMPO)
Dutch Registered NH_3 emissions	2020	$1 \text{ km} \times 1 \text{ km}$	Annual

217

218 2.4 DECSO

219 DECSO is an inversion algorithm developed for the purpose of deriving emissions of short-lived species
 220 from satellite observations. As such DECSO has been specifically designed to use daily satellite
 221 observations of column concentrations to provide rapid updates of emission estimates of short-lived
 222 atmospheric constituents on a regional scale. An extended Kalman filter is used, in which emissions are
 223 translated to column concentrations via the CTM and these are compared to the satellite column



224 observations. Based on that single forward CTM simulation, the sensitivity of concentrations to
225 emissions is calculated by using trajectory analyses to account for transport away from the source. In
226 previous studies, DECSO has been applied to NO₂ observations from different satellites including
227 TROPOMI to estimate NO_x emissions (Mijling et al., 2013; Ding et al., 2015; van der A et al., 2020;
228 Ding et al., 2022; Ding et al., 2020; van der A et al., 2024). The studies revealed that the temporal and
229 spatial variability of total surface NO_x emissions are captured well by DECSO (Ding et al., 2017b; van
230 der A et al., 2017; Liu et al., 2018). Here we have used the updated version DECSO v6.3 (van der A et
231 al., 2024) for estimating simultaneously NO_x and NH₃ emissions using the daily observations from
232 TROPOMI and CrIS (referred to as multi-species DECSO). The main changes of v6.3 include
233 improving the sensitivity matrix calculation and using the latest Eulerian regional off-line CTM
234 CHIMERE v2020v3 (Menut et al., 2021) instead of CHIMERE v2013. In the CTM, we employ the
235 Copernicus Landcover 2019 data (Buchhorn et al., 2020) , and the source sector distributions of
236 emissions obtained from HTAP v3 of 2018, which are also used as input emissions of other species
237 beside NO_x and NH₃. CHIMERE is driven by the operational meteorological forecast of the European
238 Centre for Medium-Range Weather Forecasts (ECMWF). Here we present the specific setting in
239 DECSO for NH₃ (referred to as DECSO-NH3).

240 To update NH₃ emissions based on the Kalman filter equations, one of the essential calculations is the
241 Kalman gain matrix (**K**) using the following equation:

$$242 \quad \mathbf{K} = \mathbf{P}^f(t)\mathbf{H}[\mathbf{H}\mathbf{P}^f(t)\mathbf{H}^T + \mathbf{R}]^{-1} \quad (1)$$

243 **P**^f is the error covariance matrix of the forecasted emissions at time *t*. **H** is the sensitivity matrix
244 (Jacobian) describing how the NH₃ column concentration on a satellite footprint depends on gridded
245 NH₃ emissions. **R** is the error covariance combining the observation error of tropospheric NH₃ columns,
246 the uncertainty of the CTM, and representation error introduced by projection of modelled columns on
247 the satellite footprint.

248 **P**^f is parametrised based on an evaluation of the emission forecast error *q*, which is the error increase
249 during one time step of the forecast model. The emission forecast model is persistence, predicting that
250 the emission is equal to the analysis of the emissions from the previous day. We parametrize *q* of NH₃
251 following:

$$252 \quad q = \varepsilon_{abs} \exp\left(-\frac{\varepsilon_{rel}}{\varepsilon_{abs}} e\right) + \varepsilon_{rel} e \quad (2)$$

253 ε_{abs} and ε_{rel} are the absolute and relative errors that are the dominating emission errors for low and high
254 emissions respectively.

255 To determine ε_{abs} , ε_{rel} and also the covariance matrix **R** for NH₃, we follow the method described by
256 Ding et al. (2017a) based on the analysis of Observation minus Forecast (OmF) and Observation minus



257 Assimilation (OmA). The fitted ε_{abs} , ε_{rel} are 0.075×10^{15} molecule $\text{cm}^{-2} \text{h}^{-1}$ and 0.045. Note that \mathbf{R} is the
258 variance of the observation error, the CTM model error and the representation error. Our analyses
259 showed that the \mathbf{R} values are dominated by the satellite observation errors (σ_{obs}). The representation
260 error can be neglected. We set the small contribution of model errors in \mathbf{R} to 0.5×10^{15} molecule cm^{-2} .
261 To capture the quick changes of NH_3 emissions during the fertilizing seasons and give more weight to
262 satellite observations with high values during the assimilation, we need to reduce their high observation
263 errors for high values and keep the same observation errors for low values. By fitting NH_3 observation
264 errors (σ_{obs}) against the observed columns C using all observations in 2020, we find a linear relation:

$$265 \quad \bar{\sigma}_{\text{obs}} = \alpha C + b \quad (3)$$

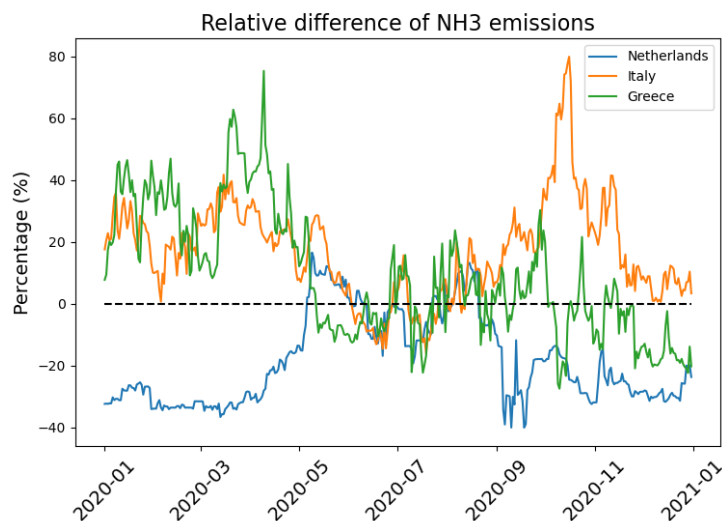
266 α is equal to 0.2 and b is equal to 1×10^{15} molecule cm^{-2} . If the given σ_{obs} is larger than $\alpha C + b$, we
267 use Eq (3) for the observation error in \mathbf{R} .

268 We update NH_3 emissions only over land since there is almost no NH_3 emissions over oceans and seas.

269 As we mentioned, NH_3 reacts with sulfuric and nitric acids from SO_2 and NO_x to form $\text{PM}_{2.5}$. The
270 changes in NO_x and SO_2 emissions will affect the concentration and removal of NH_3 in the atmosphere.

271 Inaccurate emissions of NO_x and SO_2 will therefore affect the inversion of NH_3 emissions. To assess
272 the sensitivity of NH_3 emissions derived with DECSO on NO_x and SO_2 emissions, we have run DECSO
273 with different NO_x and SO_2 emissions (default emissions of HTAP v3 and doubling the emissions of
274 HTAP v3 for SO_2 and NO_x) as input for the CTM. The results shows that the inversion of NH_3 emissions
275 is not sensitive to the change of SO_2 emissions, but it is to NO_x emissions. In Europe, the impact of SO_2
276 emissions on NH_3 can be neglected nowadays due to the low SO_2 emissions (Luo et al., 2022), which
277 have been reduced by 80% in 2020 compared to 2005 (EEA, 2023). The sensitivity tests indicate that
278 up-to-date NO_x emissions are very important for the accurate inversion of NH_3 emissions. The monthly
279 NO_x emissions of HTAP in 2018 and derived with DECSO in 2020 are quite different over the various
280 countries (Figure S3). In 2020, due to the COVID-19 pandemic, NO_x emissions reduced compared to
281 other years. van der A et al. (2024) has compared the seasonality of NO_x emissions of DECSO to other
282 bottom-up inventories and showed individual temporal variability of industrial facilities is derived with
283 DECSO in Europe, while bottom-up inventories use the same temporal profile per country per sector
284 and no detailed information of the temporal changes of individual sources. We estimate NH_3 and NO_x
285 emissions with DECSO simultaneously (the multi-specie DECSO) from CrIS and TROPOMI on a daily
286 basis. We use the DECSO-NH3 version to estimate only NH_3 emissions from CrIS and use NO_x
287 emissions of HTAP v3 as input for the CTM. Figure 1 shows the difference of monthly NH_3 emissions
288 in three countries (Netherlands, Italy and Greece) derived with the multi-species DECSO version and
289 the DECSO-NH3 version. The derived NH_3 emissions all differ largely (up to $\pm 40\%$) in winter and less
290 in summer.

291



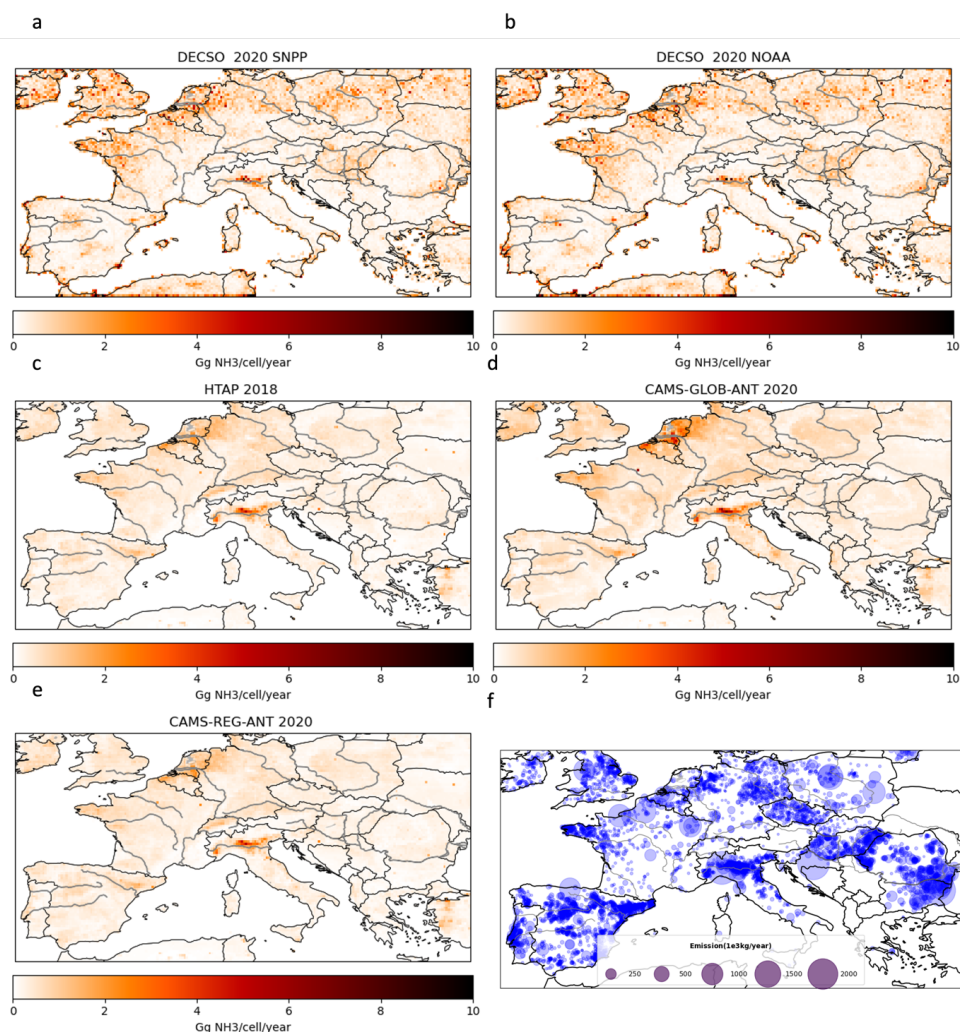
292

293 *Figure 1. The relative difference (multi-species DECSO minus DECSO-NH3) of NH₃ emissions between multi-species DECSO and*
294 *DECSO-NH3. DECSO-NH3 means that only NH₃ emissions are derived with CrIS-NOAA-20. multi-species DECSO means that*
295 *NH₃ and NO_x emissions are derived using CrIS-NOAA-20 and TROPOMI observations.*

296 3. Results

297 3.1 NH₃ emissions in Europe

298 We have run the DECSO-parallel version with NH₃ observations from CrIS-NOAA-20 and CrIS-SNPP
299 respectively to estimate NH₃ emissions over the selected domain of Europe in 2020 (Figure 2). The total
300 NH₃ emissions over the study domain are 8.0 Tg/year from SNPP and 8.1 Tg /year from NOAA-20.
301 The spatial distribution of the NH₃ emissions derived from the two satellites agrees well, with small
302 differences resulting from deviations of the observed NH₃ columns. The spatial distribution of high NH₃
303 emissions derived from DECSO is similar to that of HTAP, CAMS-REG-ANT and CAMS-GLOB-ANT
304 but with more local-scale variability and hotspots. The total emissions of DECSO over the European
305 domain are higher than HTAP (4.2 Tg/year), CAMS-REG-ANT (4.0 Tg/year) and CAMS-GLOB-ANT
306 (5.9 Tg/year)



307

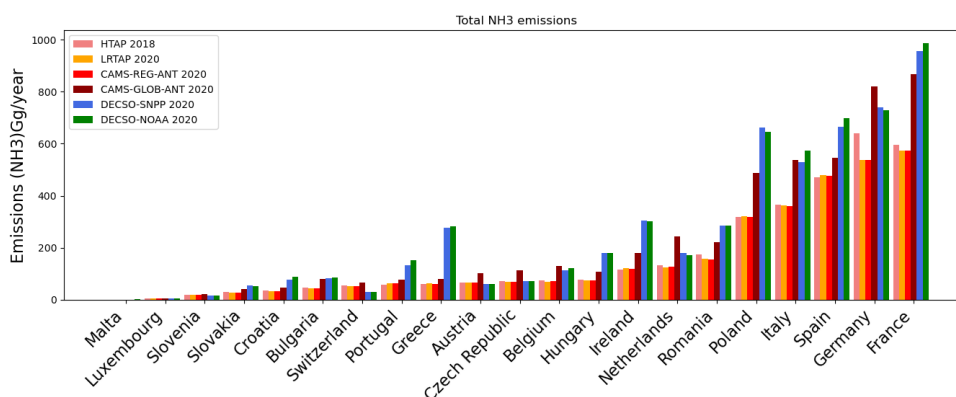
308 *Figure 2. NH₃ emission maps. NH₃ emissions derived with DECSO from (a) SNPP and (b) NOAA-20 in 2020. NH₃ emissions of*
 309 *(c) HTAP in 2018, (d) CAMS-GLOB-ANT in 2020 (e) CAMS-REG-ANT in 2020. (f) The registered point sources of E-PRTR in*
 310 *2017.*

311 The locations of high NH₃ emissions, especially in Po-Valley, Spain, Hungary and the east of Romania,
 312 shown in DECSO are highly correlated to the registered NH₃ point sources of E-PRTR which are from
 313 industrial facilities including livestock facilities but not from fertilizer applications. We see that
 314 emissions from the Netherlands are high in DECSO and the bottom-up inventories but are missing in
 315 the database of E-PRTR. For the countries in East Europe (e.g. Poland, Hungary, Romania), the NH₃
 316 emissions derived with DECSO are much higher than from the bottom-up inventories. To assess the
 317 NH₃ emissions per country, we calculated the country total emissions (see Figure 3). The correlation



318 coefficients of country totals from DECSO with the bottom-up inventories are all higher than 0.95. In
 319 general, the country totals of NH₃ emissions derived by DECSO from either NOAA-20 or SNPP are
 320 comparable to HTAP, LRTAP, CAMS-REG-ANT and CAMS-GLOB-ANT, with DECSO about 30%
 321 higher. HTAP, LRTAP and CAMS-REG-ANT have very similar emissions per country, while CAMS-
 322 GLOB-ANT shows higher emissions than the other three bottom-up inventories. Because HTAP v3
 323 uses annual emissions from CAMS-REG-ANT for Europe, the only difference between HTAP v3 and
 324 CAMS-REG-ANT is the difference in year. The input of CAMS-REG-ANT is mainly based on LRTAP.
 325 CAMS-GLOB-ANT is based on EDGAR and use different emission activities and factors compared to
 326 the other three bottom-up inventories. In the North part of Europe, for example Netherlands and
 327 Germany, DECSO results show lower NH₃ emissions than CAMS-GLOB-ANT but higher than HTAP,
 328 LRTAP and CAMS-REG-ANT.

329



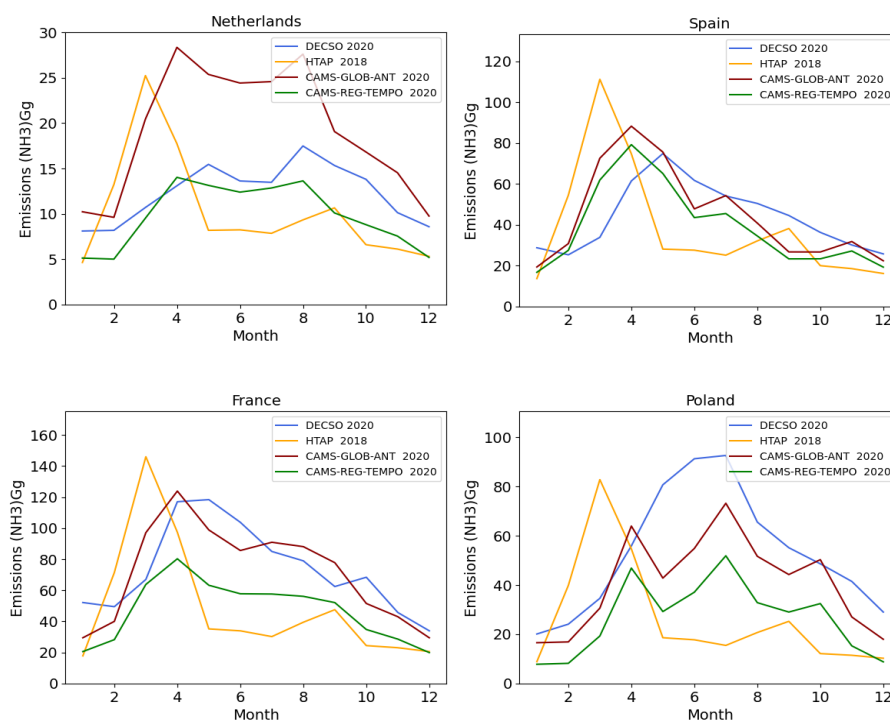
330

331 *Figure 3 Country totals of NH₃ emissions (Gg/year) according to database LRTAP in 2018, bottom-up inventories HTAP in*
 332 *2018, CAMS-REG-ANT in 2020, CAMS-GLOB-ANT in 2020 and the DECSO calculations from SNPP and NOAA-20 in 2020.*

333 To analyze the seasonality of NH₃ emissions derived from DECSO, we compare the monthly emissions
 334 of DECSO with bottom-up inventories. Figure 4 shows the monthly NH₃ emissions from DECSO,
 335 HTAP, CAMS-REG-TEMPO, and CAMS-GLOB-ANT of the Netherlands, Spain, France and Poland.
 336 We see that the seasonal cycle of NH₃ emissions of DECSO are closer to CAMS-GLOB-ANT. HTAP
 337 shows the exact same monthly variability for each country. CAMS-REG-TEMPO shows very similar
 338 monthly patterns to the ones reported by CAMS-GLOB-ANT as they are both using the same method
 339 to derive the temporal profiles for livestock and agricultural soil emissions (Guevara et al., 2021). In
 340 the Netherlands as an example for north Europe, the monthly NH₃ emissions of DECSO are lower than
 341 CAMS-GLOB-ANT but very close to CAMS-REG-ANT. Two peaks of NH₃ emissions show up in
 342 April and August for CAMS emissions. This is also confirmed by the monthly surface concentrations



343 measured by the MAN network (Figure S4). In Spain and France, the monthly emissions of DECSO
 344 are comparable to CAMS-GLOB-ANT. In the east part of Europe, such as Poland, DECSO estimates
 345 higher emissions. Note that in Spring, when the NH₃ emissions are high due to fertilizer applications
 346 on farms, the NH₃ emissions derived with DECSO can suffer from a time lag due to insufficient
 347 observations (e.g. due to cloudiness, see Figure S5).



348
 349 *Figure 4 Monthly NH₃ emissions (Gg/month) of DECSO in 2020, HTAP in 2018, CAMS-REG-TEMPO in 2020 and CAMS-GLOB-*
 350 *TEMPO in 2020 for (a) the Netherlands, (b) Spain, (c) France and (d) Poland.*

351

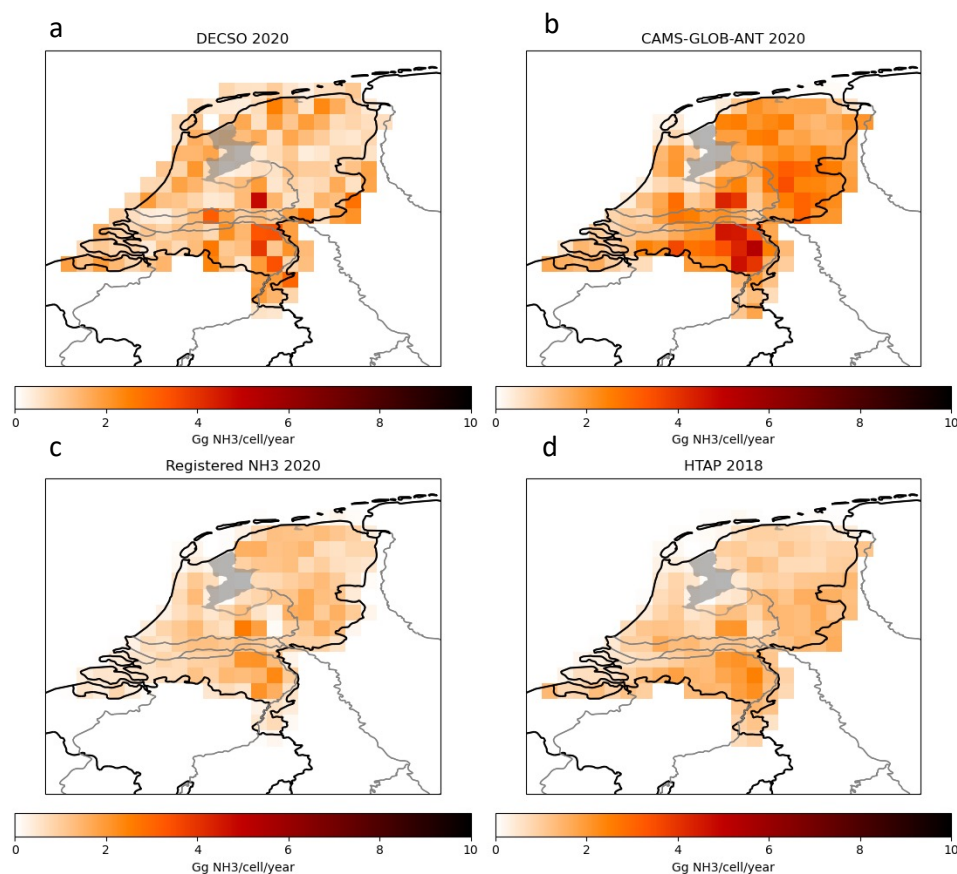
352 3.2 Emissions in the Netherlands

353 On the emission maps of Figure 2, we see that the Netherlands and Po-valley have the highest emission
 354 intensity of NH₃. In this section, we focus our analysis on the Netherlands since it has the densest
 355 network for monitoring surface NH₃ concentrations and also a detailed emission inventory on a very
 356 high spatial resolution. The total emissions of the Netherlands estimated from the two satellites are very
 357 similar (Figure 3), but the spatial distributions show significant differences (Figure S6). One possible
 358 reason is that about 10% more observations are available from NOAA-20 than SNPP in 2020 (see Figure
 359 S7). The number of valid observations is in general low at high latitudes (Figure S8). More observations
 360 allow the detection of fast changes of NH₃ emissions from day to day. By averaging the emissions, the



361 information from both satellites is combined and improved the quality of the derived emissions due to
362 a doubling of the number of observations. We use the average of the results of DECSO-SNPP and
363 DECSO-NOAA-20 to get a better spatial distribution of NH₃ emissions derived from satellite
364 observations.

365 We compare the total NH₃ emissions of DECSO with CAMS-GLOB-ANT, HTAP and official national
366 NH₃ emissions of the Netherlands, which are 148, 230, 122 and 123 Gg/year respectively. DECSO is
367 lower than CAMS-GLOB-ANT but higher than HTAP and the official NH₃ emissions of the
368 Netherlands. Figure 5 shows the spatial distribution of each inventory in the Netherlands. We see that
369 DECSO captures the high emission areas and regional distribution over the country. The correlation
370 coefficients of the spatial distribution of NH₃ emissions between DECSO and the national emissions of
371 the Netherlands, HTAP v3, CAMS-GLOB-ANT are 0.87, 0.87 and 0.88 respectively. At the resolution
372 of the individual DECSO grid cells, 0.2° × 0.2° grid cell, the emission patterns show differences. This
373 may be due to uncertainties in the location of the emissions and displacements by up to 0.5° to 1° grid
374 cell.



375

376 *Figure 5 NH_3 emissions in the Netherlands. (a) The averaged NH_3 emissions derived with DECSO from SNPP and NOAA-20.*

377 *(b) NH_3 emissions of CAMS-GLOB-ANT in 2020. (c) The official national NH_3 emissions for the Netherlands in 2020 (from*

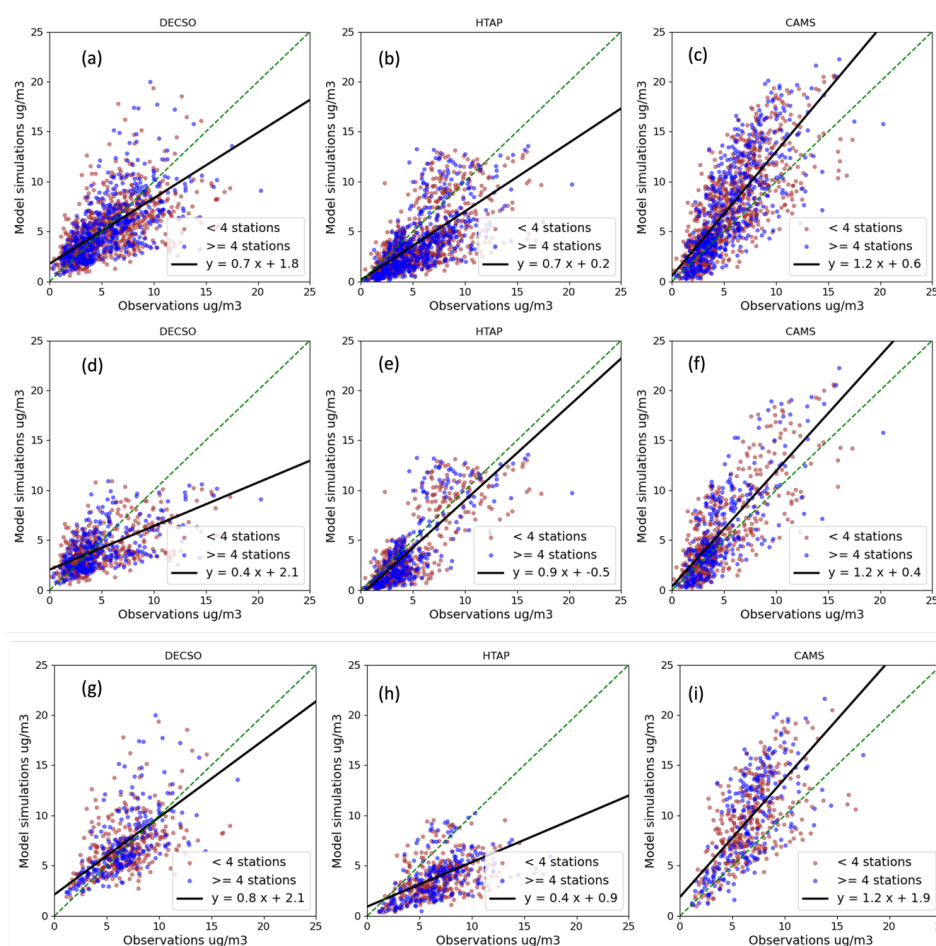
378 *emissieregistratie.nl). (d) NH_3 emissions of HTAP in 2018.*

379 To further assess the DECSO results using in-situ observations from both LML and MAN networks in
380 the Netherlands, we have conducted three runs of CHIMERE for the year 2020 using NH_3 emissions
381 from DECSO in 2020, HTAP in 2018 and CAMS-GLOB-ANT in 2020 over the European domain
382 (same as the setup of DECSO). To compare to the surface NH_3 measurement from the MAN network,
383 we calculate the monthly average of surface NH_3 concentrations from the model simulations. Figure 6
384 (a-c) shows the scatter plots of monthly NH_3 concentrations of model simulations against observations
385 for the whole year. We see that modelled NH_3 concentrations with the HTAP emissions are
386 underestimated and those with the CAMS-GLOB-ANT emissions are overestimated compared to in-
387 situ observations. The modelled NH_3 concentrations with DECSO emissions have the lowest bias
388 (Figure 7). The performance of model simulations is better in summer months (April to September)
389 than in winter months (October-March). In winter months, few cloud-free satellite observations are



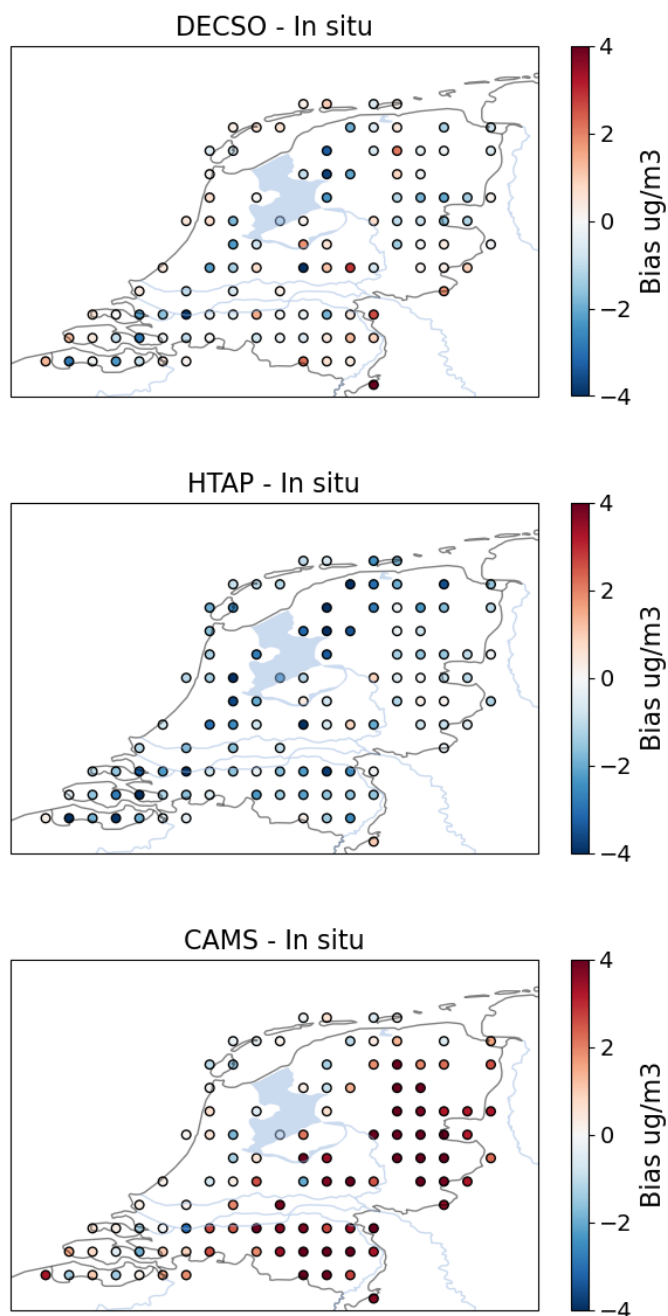
390 available for the Netherlands. For DECSO, the scatter plot looks more spread out than in summer
 391 months (Figure 6d-i). In summer months, the NH₃ concentrations with CAMS-GLOB-ANT are largely
 392 overestimated and with HTAP are largely underestimated, while DECSO has a lower bias compared to
 393 the other two. Note that in the grid cells, the number of stations can vary from 1 to 16. If we select grid
 394 cells with more than 3 sites, DECSO shows better spatial correlation with in-situ observations than for
 395 the other two inventories and the lowest bias (Figure 7 and Table 2).

396



397

398 *Figure 6. Scatter plots of observations from the MAN network with NH₃ surface concentrations from model simulations with*
 399 *NH₃ emissions from DECSO (left column), HTAP (middle column) and CAMS-GLOB-ANT (right column). (a-c) The scatter plot*
 400 *of data for the whole year for all sites. (d-f) The scatter plot of the data in winter months (October to March). (g-i) The*
 401 *scatter plot of the data in summer months (April to September). Each point presents the model grid cells having the in-situ*
 402 *observations. The red dots mean there are less than four in-situ sites in the grid cells. The blue dots mean there are at least*
 403 *four in-situ sites in the grid cell. The fitted black line is for grid cells with at least four in-situ sites.*



404

405

406

407

Figure 7. Bias of the model simulated surface concentrations with NH₃ emissions from DECSO (left column), HTAP (middle column) and CAMS-GLOB-ANT (right column) compared to the in-situ observations from the MAN network.



408 *Table 2. The spatial and temporal correlation coefficients and the bias of monthly mean simulated NH₃ surface concentration*
409 *using DECSO, HTAP and CAMS-GLOB-ANT NH₃ emissions against observations of the MAN network for grid cells with more*
410 *than three measurement locations.*

	Temporal correlation coefficient	Spatial correlation coefficient	Bias (ug/m ³)	RMSE (ug/m ³)
DECSO	0.64	0.73	-0.2	2.6
HTAP v3	0.70	0.70	-1.9	3.0
CAMS-GLOB-ANT	0.82	0.70	-0.3	3.8

411

412

413 The LML network has six sites measuring surface NH₃ concentrations, which are provided every hour.
414 Since the difference in our model simulations is only due to the monthly input emissions of NH₃, we
415 calculate monthly average NH₃ observations for the six sites to compare with the modelled monthly
416 averaged concentrations. The comparison shows that the model simulations using the DECSO NH₃
417 emissions have similar performance as bottom-up inventories (Figure S9 and S10). The correlations of
418 modelled monthly NH₃ concentration using DECSO and CAMS-GLOB-ANT emissions with the
419 observations from the LML network are better than that of HTAP, while CAMS-GLOB-ANT has the
420 lowest bias. Based on these six sites, the comparison shows that the model result using DECSO is very
421 comparable with that using CAMS-GLOB-ANT.

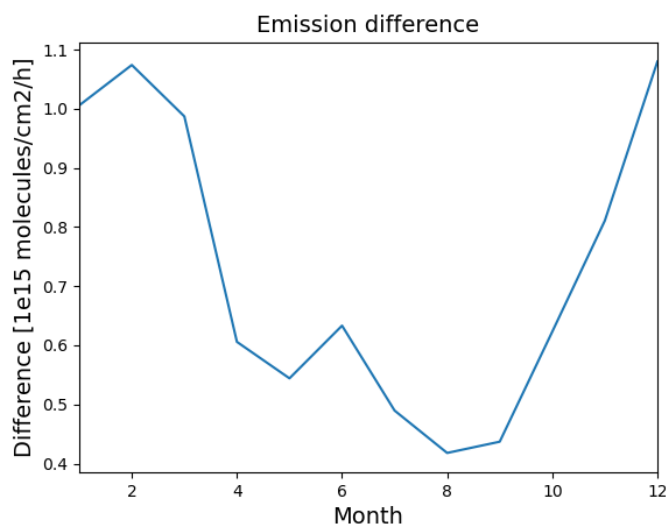
422

423 3.3 Uncertainties and bias of NH₃ emissions

424 One advantage of DECSO is that a standard deviation of derived emissions is also calculated per grid
425 cell on a daily basis according the Kalman filter equations. As described by van der A et al. (2024), the
426 derived errors in the emissions are correlated in time linked to the assumption of the persistent emission
427 forecast model. The autocorrelation effects can be neglected after about one week up to ten days. We
428 follow the autocorrelation function presented by van der A et al. (2024) to calculate the monthly variance
429 of NH₃ emissions. The monthly variance of NH₃ emissions for each grid cell in the study domain varies
430 from 17% to 58%. For the Netherlands, the precision (random uncertainty) of the monthly emissions is
431 about 20% and the precision of the annual total is about 5%.



432 A bias in satellite derived emissions can be introduced due to the linearisation of the averaging kernels
433 (Sitwell et al., 2022). The CrIS ammonia observations are retrieved in logarithm space together with
434 logarithmic averaging kernels. As discussed by Sitwell et al. (2022), either using the logarithmic
435 averaging kernel or the linearized averaging kernel introduces a bias when applying them to the model
436 simulated profiles. The logarithmic averaging kernels cause problems when the model profiles are zero
437 at any point in the profile and lead to a positive bias in emission estimates. Linearized averaging kernels
438 may introduce a negative bias in emissions when there is a large difference between the model profile
439 and the a priori profile used in the retrieval.



440

441 *Figure 8. The absolute change of monthly NH₃ emissions (molecule/cm²/h) if there is a positive bias of 5×10^{15}*
442 *molecule/cm² of each NH₃ column observation.*

443 To assess how the biases in satellite NH₃ observations affect emissions derived by DECSO, we have
444 done two simple bias tests. For the first test, the NH₃ columns of CrIS on NOAA-20 are increased by
445 20%, a positive relative bias for the satellite observations. The annual emissions of NH₃ with the
446 introduced bias increase by 27% for the European domain. It seems that the introduced bias has a higher
447 impact on emissions in winter than in summer. The relative bias on emissions can be as high as 50% in
448 winter. The change of emissions in summer becomes even negative probably because NH₃ column
449 concentrations can show a large variation from day to day. When the NH₃ columns are very high on
450 one day and next drop to a very low value, the absolute change in concentration is larger than the
451 original situation without introduced bias. This will lead to a larger decrease in the updated emissions
452 and can result in a negative change of emissions.



453 For the second test, an absolute bias of 5×10^{15} molecule/cm² is added to each NH₃ column observation
454 of CrIS on NOAA-20. Figure 8 shows the increase of NH₃ emissions caused by the absolute bias
455 introduced in the satellite observations. We see that the increase is doubled in winter compared to
456 summer, because the lifetime in winter is longer than in summer. The averaged effective lifetime
457 calculated with DECSO is about 10 hours in winter and 5 hours in summer. With the same bias of NH₃
458 columns, the impact on emissions is larger in winter than in summer.

459

460 4. Conclusions

461 To derive NH₃ emissions from satellite data, we presented an updated version of the DECSO algorithm
462 with specific settings for NH₃. Together with the improved the DECSO version for NO_x of (van der A
463 et al., 2024), we have the multi-species DECSO version to update NO_x and NH₃ emissions
464 simultaneously. In general, the removal of NH₃ in the atmosphere is affected by the amount of NO_x and
465 SO₂ emissions. For the study domain of Europe, our sensitivity study shows that the influence of
466 changes in NO_x emissions need to be considered in the inversion of NH₃ emissions in DECSO. The
467 impact of SO₂ emissions is very small and can be neglected since the SO₂ emissions are usually low in
468 Europe. Thus, to derive NH₃ emissions and to analyze the seasonal cycle and trend of NH₃ emissions
469 from satellite observations over Europe, it is recommended to include updated NO_x emissions in the
470 inversion calculation of NH₃ emissions in DECSO. For regions with high SO₂ emissions, it is necessary
471 to consider if the SO₂ emissions are changing rapidly and are up-to-date in the inversion.

472 The error covariances of the updated daily NH₃ emissions per grid cell are provided during the
473 calculation in DECSO. Considering the autocorrelations introduced by the assumption of the
474 persistency emission model, the calculated monthly error on NH₃ emissions for each grid cell in the
475 study domain varies from 17% to 58%. The yearly error per grid cell is about 5 ~ 15%. The sensitivity
476 tests for retrieval biases shows that with an introduced constant relative and absolute bias in NH₃
477 retrievals, the resulting bias in emissions derived with DECSO shows a seasonal variability with a peak
478 in winter. This means the algorithm is more sensitive to a bias in the observations during wintertime.

479 The total NH₃ emissions in our European domain derived from NH₃ observations of SNPP and NOAA-
480 20 are 8.0 Tg/year and 8.1 Tg/year respectively with a precision of about 0.2 %. The difference in
481 country total emissions derived from the two satellites is very small. However, the details of the spatial
482 distribution of emissions derived from both satellites are different over the north part of the domain,
483 such as the Netherlands. This may be due to the varying number of observations per region per year
484 from the two satellites. An average of the emissions derived from both satellites leads to an improved
485 spatial distribution compared to the emissions from the individual satellite. The spatial distribution of
486 derived NH₃ emissions is similar to the bottom-up inventories, but DECSO emissions are in general
487 higher. The annual total emissions derived by DECSO for the whole domain is larger than the bottom-



488 up inventories (LRTAP, HTAP, CAMS-REG-ANT and CAMS-GLOB-ANT). The comparison of
489 country total emissions shows that DECSO gives higher NH₃ emissions for the countries in East Europe
490 than the bottom-up inventories. In addition, DECSO results show higher sources in Spain, Hungary and
491 the east of Romania. This is in line with the registered point sources of E-PRTR. The seasonal cycle of
492 the emissions of DECSO are comparable to CAMS-GLOB-ANT, while HTAP uses the same seasonal
493 cycle for each country in Europe.

494 For the Netherlands, model simulations using NH₃ emissions from DECSO, HTAP and CAMS-GLOB-
495 ANT are compared to in-situ observations from the MAN and LML networks. In general, the simulation
496 using DECSO emissions has a lower bias, but also a lower temporal correlation compared to CAM-
497 GLOB-ANT. The performance of model simulations with DECSO is better in summer than in winter.
498 Both the bias and spatial correlation between model simulations using DECSO emissions and the MAN
499 in-situ observations are higher than CAMS-GLOB-ANT for grid cells including more than three
500 measurement sites. We conclude that satellite-derived emissions derived with DECSO show a
501 comparable temporal and spatial distribution as bottom-up inventories. The emissions derived from
502 satellite observations can provide fully independent information on emissions for verifying the bottom-
503 up inventories. With the global coverage of satellite observations, DECSO can be easily applied to
504 different regions. After validation of DECSO over regions like Europe, where there is sufficient
505 information of emissions, the added value of DECSO for deriving NH₃ emissions is to provide NH₃
506 emissions over regions with limited local information of NH₃ emissions.

507

508 Data

509 The CrIS NH₃ data v1.6.4 of SNPP and NOAA-20 created by Environment and Climate Change Canada
510 are currently publicly available upon request (mark.shephard@canada.ca) at

511 https://hpfx.collab.science.gc.ca/~mas001/satellite_ext/cris/snpp/nh3/v1_6_4.

512 The TROPOMI NO₂ data version 2.4 are available via the Copernicus website

513 <https://dataspace.copernicus.eu/> and via the TEMIS website

514 <https://www.temis.nl/airpollution/no2.php>.

515 The NH₃ and NO_x emissions of DECSO v6.3 are available on the GlobEmission website

516 <https://www.temis.nl/emissions/data.php>.

517 HTAP v3 dataset are available on https://edgar.jrc.ec.europa.eu/dataset_htap_v3

518 The European emissions data sets for countries NEC, LRTAP and large facilities E-PRTR are available
519 on the website <https://www.eea.europa.eu/en/analysis> of the EEA.



520 The CAMS databases CAMS-REG-ANT v5.1, CAMS-GLOB-ANT, CAMS-TEMPO are available on the
521 ECCAD website <https://permalink.aeris-data.fr>.

522 The NH₃ observation data from the LML network are available on the RIVM website
523 <https://data.rivm.nl/data/luchtmeetnet/>.

524 The NH₃ observation data from the MAN network are available at <https://man.rivm.nl>.

525 The Dutch registered NH₃ emissions are available at <https://data.emissieregistratie.nl/export>

526

527

528 Author contribution

529 JD developed the inversion algorithm of NH₃, performed all emission inversions, conducted the
530 analysis and wrote the manuscript. RA and JD made the improvement of the inversion algorithm of
531 NO_x. HE developed the superobservation code. ED provided the code for a linearization of the
532 averaging kernels of CrIS. MS provided the CrIS data. RWK provided the NH₃ observation data from the
533 MAN and LML networks. MGV provided the CAMS-TEMPO profiles. LT provided suggestions during the
534 research. All authors contributed to the reviewing and editing of the manuscript.

535

536 Competing interests

537 The authors declare that they have no competing interests.

538

539 Acknowledgments

540 This the work was financed by the Sentinel EO-based Emission and Deposition Service (SEEDS, Grant
541 ID 101004318) project that has received funding from the European Union's Horizon 2020 research
542 and innovation programme. Part of the work was funded by the Nationaal Kennisprogramma Stikstof
543 (NKS) of the Dutch Ministry of Agriculture, Nature and Food Quality.

544

545

546 References

547



- 548 Adams, C., McLinden, C. A., Shephard, M. W., Dickson, N., Dammers, E., Chen, J., Makar, P.,
549 Cady-Pereira, K. E., Tam, N., Kharol, S. K., Lamsal, L. N., and Krotkov, N. A.: Satellite-derived
550 emissions of carbon monoxide, ammonia, and nitrogen dioxide from the 2016 Horse River
551 wildfire in the Fort McMurray area, *Atmos. Chem. Phys.*, 19, 2577-2599, 10.5194/acp-19-
552 2577-2019, 2019.
- 553
- 554 Backes, A., Aulinger, A., Bieser, J., Matthias, V., and Quante, M.: Ammonia emissions in
555 Europe, part I: Development of a dynamical ammonia emission inventory, *Atmospheric
556 Environment*, 131, 55-66, <https://doi.org/10.1016/j.atmosenv.2016.01.041>, 2016a.
- 557
- 558 Backes, A. M., Aulinger, A., Bieser, J., Matthias, V., and Quante, M.: Ammonia emissions in
559 Europe, part II: How ammonia emission abatement strategies affect secondary aerosols,
560 *Atmospheric Environment*, 126, 153-161, <https://doi.org/10.1016/j.atmosenv.2015.11.039>,
561 2016b.
- 562
- 563 Beer, R., Shephard, M. W., Kulawik, S. S., Clough, S. A., Eldering, A., Bowman, K. W., Sander,
564 S. P., Fisher, B. M., Payne, V. H., Luo, M., Osterman, G. B., and Worden, J. R.: First satellite
565 observations of lower tropospheric ammonia and methanol, *Geophysical Research Letters*,
566 35, <https://doi.org/10.1029/2008GL033642>, 2008.
- 567
- 568 Behera, S. N., Sharma, M., Aneja, V. P., and Balasubramanian, R.: Ammonia in the
569 atmosphere: a review on emission sources, atmospheric chemistry and deposition on
570 terrestrial bodies, *Environmental Science and Pollution Research*, 20, 8092-8131,
571 10.1007/s11356-013-2051-9, 2013.
- 572
- 573 Berkhout, A. J. C., Swart, D. P. J., Volten, H., Gast, L. F. L., Haaima, M., Verboom, H., Stefess,
574 G., Hafkenscheid, T., and Hoogerbrugge, R.: Replacing the AMOR with the miniDOAS in the
575 ammonia monitoring network in the Netherlands, *Atmos. Meas. Tech.*, 10, 4099-4120,
576 10.5194/amt-10-4099-2017, 2017.
- 577
- 578 Beusen, A. H. W., Bouwman, A. F., Heuberger, P. S. C., Van Drecht, G., and Van Der Hoek, K.
579 W.: Bottom-up uncertainty estimates of global ammonia emissions from global agricultural
580 production systems, *Atmospheric Environment*, 42, 6067-6077,
581 <https://doi.org/10.1016/j.atmosenv.2008.03.044>, 2008.
- 582
- 583 Boersma, K. F., Vinken, G. C. M., and Eskes, H. J.: Representativeness errors in comparing
584 chemistry transport and chemistry climate models with satellite UV-Vis tropospheric
585 column retrievals, *Geosci. Model Dev.*, 9, 875-898, 10.5194/gmd-9-875-2016, 2016.
- 586
- 587 Buchhorn, M., Smets, B., Bertels, L., De Roo, B., Lesiv, M., Tsendbazar, N.-E., Herold, M., and
588 Fritz, S.: Copernicus Global Land Service: Land Cover 100m: collection 3: epoch 2019: Globe,
589 10.5281/zenodo.3939050, 2020.
- 590
- 591 Cao, H., Henze, D. K., Shephard, M. W., Dammers, E., Cady-Pereira, K., Alvarado, M.,
592 Lonsdale, C., Luo, G., Yu, F., Zhu, L., Danielson, C. G., and Edgerton, E. S.: Inverse modeling of
593 NH₃ sources using CrIS remote sensing measurements, *Environmental Research Letters*, 15,
594 104082, 10.1088/1748-9326/abb5cc, 2020.



- 595
596 Cao, H., Henze, D. K., Zhu, L., Shephard, M. W., Cady-Pereira, K., Dammers, E., Sitwell, M.,
597 Heath, N., Lonsdale, C., Bash, J. O., Miyazaki, K., Flechard, C., Fauvel, Y., Kruit, R. W.,
598 Feigenspan, S., Brümmner, C., Schrader, F., Twigg, M. M., Leeson, S., Tang, Y. S., Stephens, A. C.
599 M., Braban, C., Vincent, K., Meier, M., Seidler, E., Geels, C., Ellermann, T., Sanocka, A., and
600 Capps, S. L.: 4D-Var Inversion of European NH₃ Emissions Using CrIS NH₃ Measurements and
601 GEOS-Chem Adjoint With Bi-Directional and Uni-Directional Flux Schemes, *Journal of*
602 *Geophysical Research: Atmospheres*, 127, e2021JD035687,
603 <https://doi.org/10.1029/2021JD035687>, 2022.
604
605 Chen, Y., Shen, H., Kaiser, J., Hu, Y., Capps, S. L., Zhao, S., Hakami, A., Shih, J. S., Pavur, G. K.,
606 Turner, M. D., Henze, D. K., Resler, J., Nenes, A., Napelenok, S. L., Bash, J. O., Fahey, K. M.,
607 Carmichael, G. R., Chai, T., Clarisse, L., Coheur, P. F., Van Damme, M., and Russell, A. G.: High-
608 resolution hybrid inversion of IASI ammonia columns to constrain US ammonia emissions
609 using the CMAQ adjoint model, *Atmos. Chem. Phys.*, 21, 2067-2082, 10.5194/acp-21-2067-
610 2021, 2021.
611
612 Clarisse, L., Clerbaux, C., Dentener, F., Hurtmans, D., and Coheur, P.-F.: Global ammonia
613 distribution derived from infrared satellite observations, *Nature Geoscience*, 2, 479-483,
614 10.1038/ngeo551, 2009.
615
616 Crippa, M., Guizzardi, D., Muntean, M., Schaaf, E., Dentener, F., van Aardenne, J. A., Monni,
617 S., Doering, U., Olivier, J. G. J., Pagliari, V., and Janssens-Maenhout, G.: Gridded emissions of
618 air pollutants for the period 1970–2012 within EDGAR v4.3.2, *Earth Syst. Sci. Data*, 10, 1987-
619 2013, 10.5194/essd-10-1987-2018, 2018.
620
621 Crippa, M., Guizzardi, D., Butler, T., Keating, T., Wu, R., Kaminski, J., Kuenen, J., Kurokawa, J.,
622 Chatani, S., Morikawa, T., Pouliot, G., Racine, J., Moran, M. D., Klimont, Z., Manseau, P. M.,
623 Mashayekhi, R., Henderson, B. H., Smith, S. J., Suchyta, H., Muntean, M., Solazzo, E., Banja,
624 M., Schaaf, E., Pagani, F., Woo, J. H., Kim, J., Monforti-Ferrario, F., Pisoni, E., Zhang, J., Niemi,
625 D., Sassi, M., Ansari, T., and Foley, K.: The HTAP_v3 emission mosaic: merging regional and
626 global monthly emissions (2000–2018) to support air quality modelling and policies, *Earth*
627 *Syst. Sci. Data*, 15, 2667-2694, 10.5194/essd-15-2667-2023, 2023.
628
629 Dammers, E., McLinden, C. A., Griffin, D., Shephard, M. W., Van Der Graaf, S., Lutsch, E.,
630 Schaap, M., Gainairu-Matz, Y., Fioletov, V., Van Damme, M., Whitburn, S., Clarisse, L., Cady-
631 Pereira, K., Clerbaux, C., Coheur, P. F., and Erisman, J. W.: NH₃ emissions from large point
632 sources derived from CrIS and IASI satellite observations, *Atmos. Chem. Phys.*, 19, 12261-
633 12293, 10.5194/acp-19-12261-2019, 2019.
634
635 Ding, J., van der A, R. J., Mijling, B., and Levelt, P. F.: Space-based NO_x emission estimates
636 over remote regions improved in DECSO, *Atmos. Meas. Tech.*, 10, 925-938, 10.5194/amt-10-
637 925-2017, 2017a.
638
639 Ding, J., van der A, R. J., Mijling, B., Levelt, P. F., and Hao, N.: NO_x emission estimates during
640 the 2014 Youth Olympic Games in Nanjing, *Atmos. Chem. Phys.*, 15, 9399-9412,
641 10.5194/acp-15-9399-2015, 2015.



642
643 Ding, J., van der A, R., Mijling, B., de Laat, J., Eskes, H., and Boersma, K. F.: NO_x emissions in
644 India derived from OMI satellite observations, *Atmospheric Environment: X*, 14, 100174,
645 <https://doi.org/10.1016/j.aeaoa.2022.100174>, 2022.
646
647 Ding, J., van der A, R. J., Eskes, H. J., Mijling, B., Stavrou, T., van Geffen, J. H. G. M., and
648 Veefkind, J. P.: NO_x Emissions Reduction and Rebound in China Due to the COVID-19 Crisis,
649 *Geophysical Research Letters*, 47, e2020GL089912, <https://doi.org/10.1029/2020GL089912>,
650 2020.
651
652 Ding, J., Miyazaki, K., van der A, R. J., Mijling, B., Kurokawa, J. I., Cho, S., Janssens-Maenhout,
653 G., Zhang, Q., Liu, F., and Levelt, P. F.: Intercomparison of NO_x emission inventories over East
654 Asia, *Atmos. Chem. Phys.*, 17, 10125-10141, 10.5194/acp-17-10125-2017, 2017b.
655
656 Emissions of the main air pollutants in Europe, last access: 3 April, 2024.
657
658 EPRT: European Pollutant Transfer Register, database version v4.2 [dataset], 2012.
659
660 Erismann, J. W., Sutton, M. A., Galloway, J., Klimont, Z., and Winiwarter, W.: How a century of
661 ammonia synthesis changed the world, *Nature Geoscience*, 1, 636-639, 10.1038/ngeo325,
662 2008.
663
664 Erismann, J. W., Galloway, J. N., Seitzinger, S., Bleeker, A., Dise, N. B., Petrescu, A. M. R., Leach,
665 A. M., and de Vries, W.: Consequences of human modification of the global nitrogen cycle,
666 *Philosophical Transactions of the Royal Society B: Biological Sciences*, 368, 20130116,
667 doi:10.1098/rstb.2013.0116, 2013.
668
669 Eskes, H. J. and Eichmann, K.-U.: SSP Mission Performance Centre Nitrogen Dioxide
670 [L2_NO2_] Readme, Tech.rep., ESA, <https://sentinel.esa.int/documents/247904/3541451/Sentinel-5P-Nitrogen-Dioxide-Level-2-Product-Readme-File>, 2022.
671
672
673
674 Galloway, J. N., Townsend, A. R., Erismann, J. W., Bekunda, M., Cai, Z., Freney, J. R., Martinelli,
675 L. A., Seitzinger, S. P., and Sutton, M. A.: Transformation of the Nitrogen Cycle: Recent
676 Trends, Questions, and Potential Solutions, *Science*, 320, 889-892,
677 doi:10.1126/science.1136674, 2008.
678
679 Ge, X., Schaap, M., Kranenburg, R., Segers, A., Reinds, G. J., Kros, H., and de Vries, W.:
680 Modeling atmospheric ammonia using agricultural emissions with improved spatial
681 variability and temporal dynamics, *Atmos. Chem. Phys.*, 20, 16055-16087, 10.5194/acp-20-
682 16055-2020, 2020.
683
684 Gu, B., Zhang, L., Van Dingenen, R., Vieno, M., Van Grinsven, H. J., Zhang, X., Zhang, S., Chen,
685 Y., Wang, S., Ren, C., Rao, S., Holland, M., Winiwarter, W., Chen, D., Xu, J., and Sutton, M. A.:
686 Abating ammonia is more cost-effective than nitrogen oxides for mitigating
687 PM_{2.5} air pollution, *Science*, 374, 758-762, doi:10.1126/science.abf8623, 2021.
688



689 Guevara, M., Jorba, O., Tena, C., Denier van der Gon, H., Kuenen, J., Elguindi, N., Darras, S.,
690 Granier, C., and Pérez García-Pando, C.: Copernicus Atmosphere Monitoring Service
691 TEMPOral profiles (CAM5-TEMPO): global and European emission temporal profile maps for
692 atmospheric chemistry modelling, *Earth Syst. Sci. Data*, 13, 367-404, 10.5194/essd-13-367-
693 2021, 2021.
694
695 Han, Y., Revercomb, H., Cromp, M., Gu, D., Johnson, D., Mooney, D., Scott, D., Strow, L.,
696 Bingham, G., Borg, L., Chen, Y., DeSloover, D., Esplin, M., Hagan, D., Jin, X., Knuteson, R.,
697 Motteler, H., Predina, J., Suwinski, L., Taylor, J., Tobin, D., Tremblay, D., Wang, C., Wang, L.,
698 Wang, L., and Zavyalov, V.: Suomi NPP CrIS measurements, sensor data record algorithm,
699 calibration and validation activities, and record data quality, *Journal of Geophysical
700 Research: Atmospheres*, 118, 12,734-712,748, <https://doi.org/10.1002/2013JD020344>,
701 2013.
702
703 Hoesly, R. M., Smith, S. J., Feng, L., Klimont, Z., Janssens-Maenhout, G., Pitkanen, T., Seibert,
704 J. J., Vu, L., Andres, R. J., Bolt, R. M., Bond, T. C., Dawidowski, L., Kholod, N., Kurokawa, J. I.,
705 Li, M., Liu, L., Lu, Z., Moura, M. C. P., O'Rourke, P. R., and Zhang, Q.: Historical (1750–2014)
706 anthropogenic emissions of reactive gases and aerosols from the Community Emissions Data
707 System (CEDS), *Geosci. Model Dev.*, 11, 369-408, 10.5194/gmd-11-369-2018, 2018.
708
709 Janssens-Maenhout, G., Crippa, M., Guizzardi, D., Muntean, M., Schaaf, E., Dentener, F.,
710 Bergamaschi, P., Pagliari, V., Olivier, J. G. J., Peters, J. A. H. W., van Aardenne, J. A., Monni, S.,
711 Doering, U., Petrescu, A. M. R., Solazzo, E., and Oreggioni, G. D.: EDGAR v4.3.2 Global Atlas
712 of the three major greenhouse gas emissions for the period 1970–2012, *Earth Syst. Sci. Data*,
713 11, 959-1002, 10.5194/essd-11-959-2019, 2019.
714
715 Kuenen, J., Dellaert, S., Visschedijk, A., Jalkanen, J. P., Super, I., and Denier van der Gon, H.:
716 CAMS-REG-v4: a state-of-the-art high-resolution European emission inventory for air quality
717 modelling, *Earth Syst. Sci. Data*, 14, 491-515, 10.5194/essd-14-491-2022, 2022.
718
719 Li, C., Martin, R. V., Shephard, M. W., Cady-Pereira, K., Cooper, M. J., Kaiser, J., Lee, C. J.,
720 Zhang, L., and Henze, D. K.: Assessing the Iterative Finite Difference Mass Balance and 4D-
721 Var Methods to Derive Ammonia Emissions Over North America Using Synthetic
722 Observations, *Journal of Geophysical Research: Atmospheres*, 124, 4222-4236,
723 <https://doi.org/10.1029/2018JD030183>, 2019.
724
725 Liu, F., van der A, R. J., Eskes, H., Ding, J., and Mijling, B.: Evaluation of modeling NO₂
726 concentrations driven by satellite-derived and bottom-up emission inventories using in situ
727 measurements over China, *Atmos. Chem. Phys.*, 18, 4171-4186, 10.5194/acp-18-4171-2018,
728 2018.
729
730 Lolkema, D. E., Noordijk, H., Stolk, A. P., Hoogerbrugge, R., van Zanten, M. C., and van Pul, W.
731 A. J.: The Measuring Ammonia in Nature (MAN) network in the Netherlands, *Biogeosciences*,
732 12, 5133-5142, 10.5194/bg-12-5133-2015, 2015.
733



- 734 Luo, Z., Zhang, Y., Chen, W., Van Damme, M., Coheur, P. F., and Clarisse, L.: Estimating global
735 ammonia (NH₃) emissions based on IASI observations from 2008 to 2018, *Atmos. Chem.*
736 *Phys.*, 22, 10375-10388, 10.5194/acp-22-10375-2022, 2022.
737
- 738 Menut, L., Bessagnet, B., Briant, R., Cholakian, A., Couvidat, F., Mailler, S., Pennel, R., Siour,
739 G., Tuccella, P., Turquety, S., and Valari, M.: The CHIMERE v2020r1 online chemistry-
740 transport model, *Geosci. Model Dev.*, 14, 6781-6811, 10.5194/gmd-14-6781-2021, 2021.
741
- 742 Menut, L., Bessagnet, B., Khvorostyanov, D., Beekmann, M., Blond, N., Colette, A., Coll, I.,
743 Curci, G., Foret, G., Hodzic, A., Mailler, S., Meleux, F., Monge, J. L., Pison, I., Siour, G.,
744 Turquety, S., Valari, M., Vautard, R., and Vivanco, M. G.: CHIMERE 2013: a model for regional
745 atmospheric composition modelling, *Geosci. Model Dev.*, 6, 981-1028, 10.5194/gmd-6-981-
746 2013, 2013.
747
- 748 Mijling, B. and van der A, R. J.: Using daily satellite observations to estimate emissions of
749 short-lived air pollutants on a mesoscopic scale, *Journal of Geophysical Research:*
750 *Atmospheres*, 117, 10.1029/2012JD017817, 2012.
751
- 752 Mijling, B., van der A, R. J., and Zhang, Q.: Regional nitrogen oxides emission trends in East
753 Asia observed from space, *Atmos. Chem. Phys.*, 13, 12003-12012, 10.5194/acp-13-12003-
754 2013, 2013.
755
- 756 Noordijk, H., Braam, M., Rutledge-Jonker, S., Hoogerbrugge, R., Stolk, A. P., and van Pul, W.
757 A. J.: Performance of the MAN ammonia monitoring network in the Netherlands,
758 *Atmospheric Environment*, 228, 117400, <https://doi.org/10.1016/j.atmosenv.2020.117400>,
759 2020.
760
- 761 Pinterits, M., B. Ullrich, T. Bartmann and M. Gager: European Union emission inventory
762 report 1990-2019 under the UNECE Convention on Long-range Transboundary Air Pollution
763 (Air Convention), EEA Report No 5/2021, 2021NEC, Air pollution in Europe: 2023 reporting
764 status under the National Emission reduction Commitments Directive, 2023
765 ([https://www.eea.europa.eu/publications/national-emission-reduction-commitments-](https://www.eea.europa.eu/publications/national-emission-reduction-commitments-directive-2023/air-pollution-in-europe-2023)
766 [directive-2023/air-pollution-in-europe-2023](https://www.eea.europa.eu/publications/national-emission-reduction-commitments-directive-2023/air-pollution-in-europe-2023)), 2023.
767
- 768 Renard, J. J., Calidonna, S. E., and Henley, M. V.: Fate of ammonia in the atmosphere—a
769 review for applicability to hazardous releases, *Journal of Hazardous Materials*, 108, 29-60,
770 <https://doi.org/10.1016/j.jhazmat.2004.01.015>, 2004.
771
- 772 Rijdsdijk, P., Eskes, H., Dingemans, A., Boersma, F., Sekiya, T., Miyazaki, K., and Houweling, S.:
773 Quantifying uncertainties of satellite NO₂ superobservations for data assimilation and model
774 evaluation, *EGUsphere*, 2024, 1-42, 10.5194/egusphere-2024-632, 2024.
775
- 776 Schaap, M., van Loon, M., ten Brink, H. M., Dentener, F. J., and Builtjes, P. J. H.: Secondary
777 inorganic aerosol simulations for Europe with special attention to nitrate, *Atmos. Chem.*
778 *Phys.*, 4, 857-874, 10.5194/acp-4-857-2004, 2004.
779



- 780 Shephard, M. W. and Cady-Pereira, K. E.: Cross-track Infrared Sounder (CrIS) satellite
781 observations of tropospheric ammonia, *Atmos. Meas. Tech.*, 8, 1323-1336, 10.5194/amt-8-
782 1323-2015, 2015.
- 783
- 784 Shephard, M. W., Dammers, E., Cady-Pereira, K. E., Kharol, S. K., Thompson, J., Gainariu-
785 Matz, Y., Zhang, J., McLinden, C. A., Kovachik, A., Moran, M., Bittman, S., Sioris, C. E., Griffin,
786 D., Alvarado, M. J., Lonsdale, C., Savic-Jovicic, V., and Zheng, Q.: Ammonia measurements
787 from space with the Cross-track Infrared Sounder: characteristics and applications, *Atmos.*
788 *Chem. Phys.*, 20, 2277-2302, 10.5194/acp-20-2277-2020, 2020.
- 789
- 790 Sitwell, M., Shephard, M. W., Rochon, Y., Cady-Pereira, K., and Dammers, E.: An ensemble-
791 variational inversion system for the estimation of ammonia emissions using CrIS satellite
792 ammonia retrievals, *Atmos. Chem. Phys.*, 22, 6595-6624, 10.5194/acp-22-6595-2022, 2022.
- 793
- 794 Soulie, A., C. Granier, S. Darras, N. Zilbermann, T. Doumbia, M. Guevara, J.-P. Jalkanen, S.
795 Keita, C. Liousse, M. Crippa, D. Guizzardi, R. Hoesly, and Smith, S. J.: Global Anthropogenic
796 Emissions (CAM5-GLOB-ANT) for the Copernicus Atmosphere Monitoring Service Simulations
797 of Air Quality Forecasts and Reanalyses, *Earth Syst. Sci. Data*, 2023.
- 798
- 799 Van Damme, M., Clarisse, L., Whitburn, S., Hadji-Lazaro, J., Hurtmans, D., Clerbaux, C., and
800 Coheur, P.-F.: Industrial and agricultural ammonia point sources exposed, *Nature*, 564, 99-
801 103, 10.1038/s41586-018-0747-1, 2018.
- 802
- 803 Van Damme, M., Clarisse, L., Franco, B., Sutton, M. A., Erisman, J. W., Wichink Kruit, R., van
804 Zanten, M., Whitburn, S., Hadji-Lazaro, J., Hurtmans, D., Clerbaux, C., and Coheur, P.-F.:
805 Global, regional and national trends of atmospheric ammonia derived from a decadal (2008–
806 2018) satellite record, *Environmental Research Letters*, 16, 055017, 10.1088/1748-
807 9326/abd5e0, 2021.
- 808
- 809 van der A, R. J., Ding, J., and Eskes, H.: Monitoring European anthropogenic NO_x emissions
810 from space, *EGUsphere*, 2024, 1-20, 10.5194/egusphere-2023-3099, 2024.
- 811
- 812 van der A, R. J., de Laat, A. T. J., Ding, J., and Eskes, H. J.: Connecting the dots: NO_x emissions
813 along a West Siberian natural gas pipeline, *npj Climate and Atmospheric Science*, 3, 16,
814 10.1038/s41612-020-0119-z, 2020.
- 815
- 816 van der A, R. J., Mijling, B., Ding, J., Koukouli, M. E., Liu, F., Li, Q., Mao, H., and Theys, N.:
817 Cleaning up the air: effectiveness of air quality policy for SO₂ and NO_x emissions in China,
818 *Atmos. Chem. Phys.*, 17, 1775-1789, 10.5194/acp-17-1775-2017, 2017.
- 819
- 820 van der Graaf, S., Dammers, E., Segers, A., Kranenburg, R., Schaap, M., Shephard, M. W., and
821 Erisman, J. W.: Data assimilation of CrIS NH₃ satellite observations for improving
822 spatiotemporal NH₃ distributions in LOTOS-EUROS, *Atmos. Chem. Phys.*, 22, 951-972,
823 10.5194/acp-22-951-2022, 2022.
- 824
- 825 van Geffen, J. H. G. M., Eskes, H. J., Boersma, K. F., and Veefkind, J. P.: TROPOMI ATBD of the
826 total and tropospheric NO₂ data products, Report S5P-KNMI-L2-0005-RP, version 2.4.0,



827 202207-11, KNMI, De Bilt, The Netherlands,,
828 <https://sentinel.esa.int/documents/247904/2476257/Sentinel-5P-TROPOMI-ATBD-NO2->
829 [data-products](#) (last access: 23 Nov. 2023), 2022.
830
831 Veefkind, J. P., Aben, I., McMullan, K., Förster, H., de Vries, J., Otter, G., Claas, J., Eskes, H. J.,
832 de Haan, J. F., Kleipool, Q., van Weele, M., Hasekamp, O., Hoogeveen, R., Landgraf, J., Snel,
833 R., Tol, P., Ingmann, P., Voors, R., Kruizinga, B., Vink, R., Visser, H., and Levelt, P. F.: TROPOMI
834 on the ESA Sentinel-5 Precursor: A GMES mission for global observations of the atmospheric
835 composition for climate, air quality and ozone layer applications, *Remote Sensing of*
836 *Environment*, 120, 70-83, <http://dx.doi.org/10.1016/j.rse.2011.09.027>, 2012.
837
838 White, E., Shephard, M. W., Cady-Pereira, K. E., Kharol, S. K., Ford, S., Dammers, E., Chow, E.,
839 Thiessen, N., Tobin, D., Quinn, G., O'Brien, J., and Bash, J.: Accounting for Non-Detects:
840 Application to Satellite Ammonia Observations, *Remote Sensing*, 15, 2610, 2023.
841
842 Wyer, K. E., Kelleghan, D. B., Blanes-Vidal, V., Schauburger, G., and Curran, T. P.: Ammonia
843 emissions from agriculture and their contribution to fine particulate matter: A review of
844 implications for human health, *Journal of Environmental Management*, 323, 116285,
845 <https://doi.org/10.1016/j.jenvman.2022.116285>, 2022.
846
847 Zavalov, V., Esplin, M., Scott, D., Esplin, B., Bingham, G., Hoffman, E., Lietzke, C., Predina, J.,
848 Frain, R., Suwinski, L., Han, Y., Major, C., Graham, B., and Phillips, L.: Noise performance of
849 the CrIS instrument, *Journal of Geophysical Research: Atmospheres*, 118, 13,108-113,120,
850 <https://doi.org/10.1002/2013JD020457>, 2013.
851
852 Zhang, L., Chen, Y., Zhao, Y., Henze, D. K., Zhu, L., Song, Y., Paulot, F., Liu, X., Pan, Y., Lin, Y.,
853 and Huang, B.: Agricultural ammonia emissions in China: reconciling bottom-up and top-
854 down estimates, *Atmos. Chem. Phys.*, 18, 339-355, 10.5194/acp-18-339-2018, 2018.
855
856 Zhang, X., Gu, B., van Grinsven, H., Lam, S. K., Liang, X., Bai, M., and Chen, D.: Societal
857 benefits of halving agricultural ammonia emissions in China far exceed the abatement costs,
858 *Nature Communications*, 11, 4357, 10.1038/s41467-020-18196-z, 2020.
859
860 Zhu, L., Henze, D. K., Cady-Pereira, K. E., Shephard, M. W., Luo, M., Pinder, R. W., Bash, J. O.,
861 and Jeong, G.-R.: Constraining U.S. ammonia emissions using TES remote sensing
862 observations and the GEOS-Chem adjoint model, *Journal of Geophysical Research:*
863 *Atmospheres*, 118, 3355-3368, <https://doi.org/10.1002/jgrd.50166>, 2013.
864
865
866